Contents lists available at ScienceDirect

Applied Catalysis B: Environmental

Microkinetic modeling of H_2SO_4 formation on Pt based diesel oxidation catalysts

Hom N. Sharma[*], Yunwei Sun, Elizabeth A. Glascoe

Lawrence Livermore National Laboratory, 7000 East Ave., Livermore, CA, 94550, United States

ABSTRACT

The presence of water vapor and sulfur oxides in diesel engine exhaust leads to the formation of sulfuric acid (H_2SO_4), which severely impacts the performance of Pt/Pd based emissions aftertreatment catalysts. In this study, a microkinetic model is developed to investigate the reaction pathways of H_2SO_4 formation on Pt based diesel oxidation catalysts (DOCs). The microkinetic model consists of 14 elementary step reactions (7 reversible pairs) and yields prediction in excellent agreement with data obtained from experiments at practically relevant sulfur oxides environment in engine exhaust. The model simulation utilizing a steady-state plug flow reactor demonstrates that it matches experimental data in both kinetically and thermodynamically controlled regions. Results clearly show the negative impact of SO_3 on the SO_2 oxidation light-off temperature, consistent with experimental observations. A reaction pathway analysis shows that the primary pathway of sulfuric acid formation on Pt surface involves $SO_2{}^*$ oxidation to form $SO_3{}^*$ with the subsequent interaction of $SO_3{}^*$ with H_2O^* to form $H_2SO_4{}^*$.

1. Introduction

Sulfuric acid (H_2SO_4) formation is a detrimental, yet prevalent reaction due to interactions of sulfur oxides and water on current state-of-the-art Pt/Pd based diesel oxidation catalysts (DOC) [1–3]. Once formed, H_2SO_4 poisons the DOC, increases particulate matter (PM) formation in the engine exhaust, and creates environmental problems such as acid rain formation [1,2,4]. In addition, it is detrimental to aftertreatment units in diesel engine exhaust systems, such as the selective catalytic reduction (SCR), the lean-NO_x trap, and the continuously regenerating trap (CRT) [5]. Formation of H_2SO_4 has been attributed to the oxidation pathways of sulfur in diesel fuel and lubricants (i.e., oxidation to SO_2 in the engine and further oxidation to SO_3 at the DOC due to the excess oxygen ($\sim$12%) in the exhaust). Presence of excess water vapor (up to $\sim$7%) accelerates H_2SO_4 formation in the engine exhaust [1,3,6]. In spite of low concentrations ($\sim$1 ppm) of sulfur oxides (SO_x) in diesel engine exhaust, due to the use of ultra-low sulfur diesel fuel mandated by the U.S. Environmental Protection Agency regulations, formation of H_2SO_4 is still observed. Understanding the reaction kinetics and pathways of H_2SO_4 formation is required for a robust design and development of sulfur resistant emission aftertreatment catalysts.

Thermodynamically, formation of H_2SO_4 is exothermic; the overall reaction equation and corresponding enthalpy [7] are:

$$SO_3 + H_2O \rightarrow H_2SO_4 \quad \Delta H = -21.5 \text{ kcal mol}^{-1} \tag{1}$$
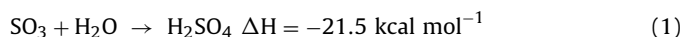
Prior studies suggest that the formation of SO_3 is extremely fast and highly favored on Pt. The SO_3 then interacts with metal or metal oxide catalysts leading to the formation of catalytically non-active metal sulfates [6,8,9]. The large binding strength of SO_3 on Pt or oxidized-Pd surfaces is one of the descriptors for the sulfation of DOC [9]. Thus, the SO_3-metal reactions eliminate the active sites of DOC from further reactions. Hence, for a complex system involving H_2O, oxygen, and sulfur oxides the reaction mechanisms and pathways are not fully understood.

Earlier experimental and modeling studies indicate that the reaction of SO_3 and H_2O is the primary route for H_2SO_4 production [10–13]. For example, in the fuel lean condition, as experienced by the DOC, oxidation of sulfur oxides is the favored path and a precursor step for the H_2SO_4 aerosol generation [14]. Phillips et al. discovered a SO_3–H_2O complex in the gas phase using microwave spectroscopy [10]. Lovejoy et al. demonstrated that the rate of H_2SO_4 formation is influenced by H_2O concentration [11]. DFT-based predictions showed a decrease in the activation energy for the reaction of SO_3 and H_2O with an increase in water coverage on the Pd(111) surface. On the other hand, in an ab-initio method based the electro-oxidation study of SO_2 on Pt(111), Kriek et al. [15] proposed H_2SO_4 formation via the HSO_3 pathway in addition

* Corresponding author.
E-mail address: sharma11@llnl.gov (H.N. Sharma).

to the SO_3 pathway. Unfortunately, prior kinetic modeling has been limited to SO_2 oxidation resulting in SO_3 formation [6,12,13,16]. Clearly the presence of H_2O in the exhaust makes the SO_x surface chemistry complex. Since complete removal of the sulfur from the fuel and lubricants is not economically viable, understanding the SO_x and H_2O chemistry in the DOCs and other systems is crucial to the development of a mitigation strategy and requires an immediate attention.

In this study, a microkinetic model is developed for H_2SO_4 formation on Pt surface that includes oxidation and H_2O interaction of sulfur oxides (SO_2 and SO_3). A microkinetic modeling approach allows us to calculate the catalytic rates, conversion, and selectivity under a given set of conditions without *a priori* assumptions of rate limiting steps or the most abundant reaction intermediate (MARI). Previously developed SO_2 oxidation microkinetic model [6,8] on Pt is extended to include SO_3 and H_2O interactions and develop a detailed understanding of the reaction pathways en route to the sulfuric acid formation. Furthermore, the analysis of HSO_3 route of H_2SO_4 formation proposed by Kriek et al. [15] shows that the pathway is not favorable under DOC conditions. The model agrees well with experimental results generated under practically relevant DOC conditions such as low emissions concentrations (ppm level), high flow rate, and high oxygen and/or water concentrations.

2. Microkinetic model

2.1. Mechanism development

The reduced surface reaction mechanism for SO_2 oxidation was adapted from previous work [6,8]. The reaction mechanism was extended to include H_2O interaction with SO_x to form H_2SO_4. In this analysis, several reactions were found to have no effect on the overall reaction progress. These eliminated reactions and the reasons for eliminating them are discussed here.

In the literature [5,15,17,18] there are two proposed pathways (i.e., Path A and Path B) involving either an SO_3^* or an HSO_3^* intermediate as shown below. Here, * indicates a vacant site; whereas the superscript * indicates an adsorbed species.

Path A:

$$SO_2^* + O^* \rightarrow SO_3^* + * \qquad (2)$$

$$SO_3^* + H_2O^* \rightarrow H_2SO_4^* + * \qquad (3)$$

Path B:

$$SO_2^* + OH^* \rightarrow HSO_3^* + * \qquad (4)$$

$$HSO_3^* + OH^* \rightarrow H_2SO_4^* + * \qquad (5)$$

Using the Unity Bond Index-Quadratic Exponential Potential (UBI-QEP) method [19,20] (see Appendix A), activation energies were computed for Paths A and B in the highly oxidizing environment and in the temperature range (<400 °C) of interest in this study. Our analysis showed that the activation barrier for HSO_3 formation in Path B (Eq. (4)) is too high ($E_a = \sim 33$ kcal mol^{-1} at 300 K) to compete with the SO_3 formation in Path A (Eq. (2), $E_a = \sim 22$ kcal mol^{-1}). Thus, inclusion of Path B has no effect on the mechanism performance for the temperature range and emissions exhaust conditions considered here. Furthermore, no evidence of formation of HSO_3 and H_2 (possibly via $OH^* \rightarrow H^* + O^*$ or $H_2O^* \rightarrow OH^* + H^*$ to form H^* species and via $2H^* \rightarrow H_2 + 2^*$ to form H_2) was reported during experiments conducted under practically relevant conditions [21]. It is noted that if the elevated temperature operation and environments differ significantly from the DOC operating conditions, the reactions in Path B may need to be considered.

Analysis showed that the reaction for water dissociation using oxygen ($H_2O^* + O^* \rightarrow 2OH^*$) reaction is feasible (activation energy,

$E_a = 9.2$ kcal mol^{-1} at 300 K [22]) in the temperature range studied. However, our work here indicates that this reaction also has no effect on the overall model performance. Therefore, these reactions are not included in the final proposed mechanism.

The reactions that were considered in this mechanism are chosen based on the reactants, possible intermediates, products, and the experimentally observed/proposed pathways [10,15]. Initially, the following seven surface species in the mechanism were considered: SO_2^*, SO_3^*, O^*, H_2O^*, OH^*, HSO_3^*, and $H_2SO_4^*$. Adsorption/desorption steps of gas phase species (i.e., O_2, SO_2, SO_3, H_2O, and H_2SO_4) and surface reactions for SO_2 oxidation and SO_3 hydration were considered. The proposed final reaction mechanism consists of 14 elementary steps (7 reversible) reactions as listed in Table 1.

2.2. Parameter estimation

Kinetic parameters such as sticking coefficients, pre-exponential factors, binding energies, and activation energies for the elementary step reactions were estimated/extracted using a combined approach, i.e., extraction from surface science experiments in literature, estimation using the semi-empirical UBI-QEP method [19,20], or estimation from the first principles quantum mechanical Density Functional Theory (DFT) calculations [8]. Sticking coefficients for the adsorption reactions were taken from values reported in literature, otherwise the initial estimate was taken as unity. Pre-exponential factors were taken as initial estimates based on Transition State Theory (TST), e.g., 10^{13} s^{-1} for desorption and 10^{11} s^{-1} for Langmuir–Hinshelwood type surface reactions [23]. For SO_2 oxidation reaction, DFT estimates of forward and backward pre-exponential factors from our previous study were used [8]. A site density (σ) of 1.5×10^{15} sites cm^{-2} (2.5×10^{-9} mol cm^{-2}) was used in our simulations based on the estimate that Pt(111) is the most stable facet [22]. Species binding energies were based on experimental or DFT values from our previous study [8] and this work. The binding energies of HSO_3 and H_2SO_4 on Pt (111) were estimated in this work using DFT implemented in VASP [24,25] (see Appendix A for details). Binding energies are coverage (θ) and temperature (T) dependent, as shown in Eq. (6). This formalism was introduced to ensure thermodynamic consistency in a surface reaction mechanism with respect to the gas phase thermodynamics

$$Q(T) = Q(T_o) - \alpha\theta - \gamma R(T - T_o) \qquad (6)$$

Here, α is the coverage dependence coefficient (kcal mol^{-1} ML^{-1}), θ is the coverage of species (ML), γ is the temperature dependence coefficient for binding energies (unitless) calculated based on statistical mechanics, R is the universal gas constant (kcal mol^{-1} K^{-1}), and T is the temperature (K). T_o is taken as 300 K. Coverage and temperature dependent activation energies were calculated on-the-fly using the UBI-QEP method. Details of the α, γ, and UBI-QEP based activation energy calculations can be found in our previous papers [6,8,22].

2.3. Reactor modeling

Steady state isothermal plug flow reactor (PFR) modeling was used to simulate the monolith scale experiments conducted in various operating conditions [12,21]. The oxidation of dilute concentrations of exhaust emission gases (i.e., ppm levels) generates very little heat, thus the isothermal assumption is reasonable and justified. The governing equations for steady state PFR are given as:

Mass balance:

$$\frac{dY_k}{dz} = \frac{G_k M_k}{\rho \ \mu} + \left(\frac{A_c}{V_R}\right) \frac{S_k M_k}{\rho \ \mu} \ \forall \ k = 1, \ldots, n_{gas} \qquad (7)$$

Table 1
Elementary step reaction mechanisms considered for SO_2 oxidation and H_2SO_4 formation on Pt.[a]

No.	Reactions	Bond index[b] (BI) [unitless]	Sticking coefficient [unitless] or Pre exponential factor [s^{-1}]	Activation energy at 300 K [kcal mol^{-1}]
Adsorption/desorption				
R_1	$O_2 + 2^* \rightarrow 2O^*$	0.5	0.05[d]	0.0
R_2	$2O^* \rightarrow O_2 + 2^*$		1×10^{13}	$52.9 - 26.6\theta_O + f(T)$
R_3	$SO_2 + ^* \rightarrow SO_2^*$	0.5	0.5[d]	0.0
R_4	$SO_2^* \rightarrow SO_2 + ^*$		1×10^{16}	$29.3 - 2.5R\Delta T$
R_5	$SO_3 + ^* \rightarrow SO_3^*$	0.5	0.5	0.0
R_6	$SO_3^* \rightarrow SO_3 + ^*$		1×10^{13}	$34.2 - 2.5R\Delta T$
R_7	$H_2SO_4 + ^* \rightarrow H_2SO_3^*$	0.5	1.0	0.0
R_8	$H_2SO_4^* \rightarrow H_2SO_4 + ^*$		1×10^{13}	$2.8 - 3.0R\Delta T$
R_9	$H_2O + ^* \rightarrow H_2O^*$	0.5	1.0[d]	0.0
R_{10}	$H_2O^* \rightarrow H_2O + ^*$		1×10^{13}	$10.27 - 2.5R\Delta T$
SO_x oxidation				
R_{11}	$SO_3^* + ^* \rightarrow SO_2^* + O^*$	0.97[c]	1.2×10^{11}	$23.2 + f(\theta_O, T)$
R_{12}	$SO_2^* + O^* \rightarrow SO_3^* + ^*$		5×10^{12}	$21.3 + f(\theta_O, T)$
H_2O reactions				
R_{13}	$SO_3^* + H_2O^* \rightarrow H_2SO_4^* + ^*$	0.5	1×10^{11}	$0.0 + f(T)$
R_{14}	$H_2SO_4^* + ^* \rightarrow SO_3^* + H_2O^*$		1×10^{11}	$19.1 + f(T)$

^a θ_O represents the oxygen surface coverage; * indicates a vacant site; whereas the superscript * indicates an adsorbed species. The functional form 'f' in the activation energy includes coverage and temperature dependence. Coverage dependence originates from the use of UBI-QEP for the estimation of activation energies, whereas the temperature dependence is derived from the statistical mechanics based calculations for degrees of freedom lost/gained upon adsorption. $\Delta T = T - T_0$, where T_0 is taken as 300 K.

^b Bond index represents the position of the transition state along the reaction coordinate, which is also used to compute the activation energies in the UBI-QEP formalism. It is defined for a reaction pair in the forward direction only. It ranges between 0 and 1, with a typical estimate of 0.5.

^c Bond index for reaction pair R_{11}–R_{12} is taken from Ref. [8].

^d Sticking coefficients for O_2, SO_2, and SO_3 are taken from Ref. [8], whereas that of H_2O is taken from Ref. [22].

Surface species balance:

$$S_k = 0, \quad \text{for k} = n_{gas} + 1, \ldots, \ n_{gas} + n_{surf}$$

$$\text{i.e.,} \quad \frac{d\theta_k}{dt} = \sum \text{Rate}_j = 0 \qquad (8)$$

Site balance:

$$\sum \theta_i = 1 \text{ for k} = n_{gas} + 1, \ldots, n_{gas} + n_{surf} \qquad (9)$$

where, k indicates the species index, n_{gas} is the number of gas phase species, n_{surf} is the number of surface species, z is the reactor length variable, Y_k is the mass fraction of gas phase species, G_k is rate of gas phase species, M_k is the molecular weight of species, S_k is the catalytic rate of gas phase species (through adsorption and desorption), ρ is the mass density, μ is the velocity, A_c/V_R is the catalyst area per unit reactor volume, and θ_i is the coverage of surface species.

Surface coverages at the reactor inlet were estimated using transient simulations until steady state coverage was achieved, thus satisfying the condition given by Eq. (8). These coverages were then utilized as initial values for the steady state simulation. The GRI Mech 3.0 gas phase reaction mechanism [26] was used to account for the gas phase chemistry. The resulting set of differential and algebraic (DAE) equations was solved using the DDASPK solver [27].

2.4. Model performance

It is expected that the microkinetic model should perform well against the experiments operated under practically relevant conditions such as atmospheric pressure, dilute emissions concentrations (ppm level), and short residence times. However, some minor parameter tuning is necessary given the pressure gap (UHV vs. atmospheric), materials gap (single crystals vs. polycrystalline and supported catalysts), and uncertainty/error associated with the experimental data. Here, monolith scale experimental data [21,12] reported in the literature are used to check the microkinetic model performance. Specifically, monolith scale experiments with three different types of reactor feed conditions are used: (a) SO_2 and O_2, (b) SO_2, O_2, and SO_3, and (c) SO_2, O_2, and H_2O. These experi-
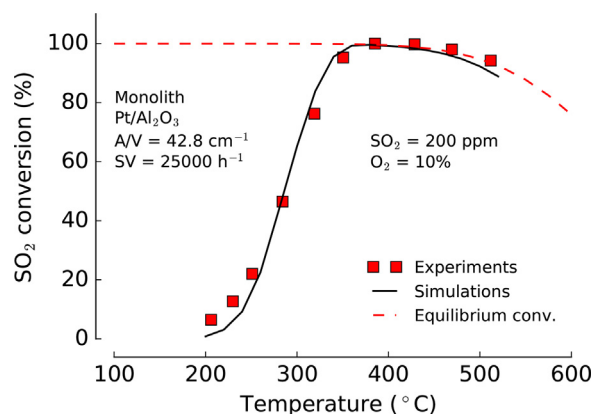

Fig. 1. Experimental data (symbols), microkinetic model performance (solid line) and calculated equilibrium conversion profile (dashed line) for SO_2 oxidation on Pt/Al$_2$O$_3$ monolith. Operating conditions: [12,21] feed of 200 ppm SO_2, 10% O_2, balance N_2; space velocity of 25,000 h^{-1}; Pt loading = 50 g ft^{-3} with 6% dispersion; catalyst length = 3.86 cm with a cell density of 325 channels inch^{-2}; and catalyst area per unit reactor volume of 46.8 cm^{-1}; total gas flow rate = 4.6 L min^{-1}.

ments were conducted in the absence of other gas species (e.g., CO, CO_2, HC, NO_x) typically present in diesel engine exhaust. Details of the mechanism performance and analysis of reaction paths are presented in Section 3.

3. Results and discussion

3.1. SO_2 oxidation

The microkinetic model was validated against experiments [12] conducted using Pt/Al$_2$O$_3$ monolith under isothermal and steady state reactor conditions. The experimental data, model simulations, and the computed theoretical equilibrium conversion profile are shown in Fig. 1. Overall, the model captures the experimental data very well over the entire temperature interval considered. A slight under prediction of SO_2 conversion at the beginning of the reaction can be attributed to the binding energy parameters as the most stable configurations of the surface species on the Pt(111) surface
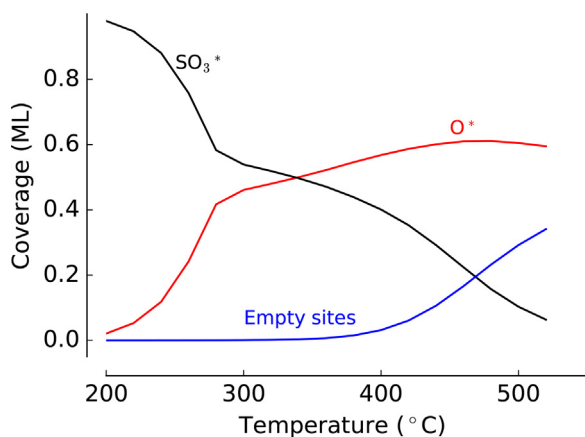
Fig. 2. Simulated steady state coverage profiles at the reactor exit. Experimental conditions are same as in Fig. 1.
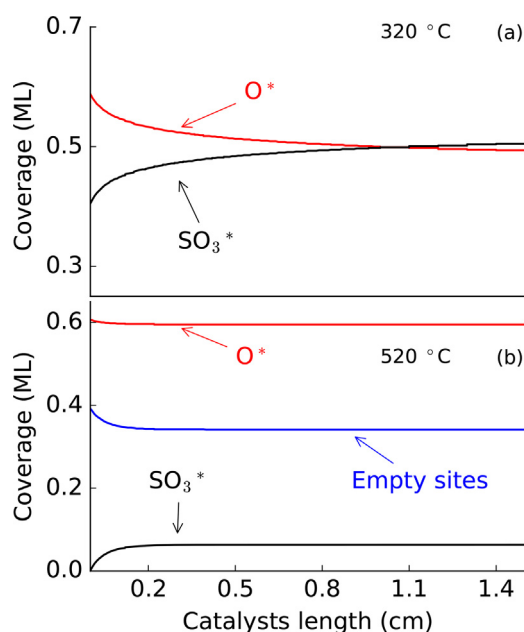

Fig. 3. Simulated axial coverage profiles at 320 °C and 520 °C, respectively. Actual catalyst length is 3.86 cm. Experimental conditions are same as in Fig. 1.

Fig. 4. Reaction path analysis (RPA) at the reactor exit at (a) 320 °C and (b) 520 °C. Only the net reaction progress is shown here. Experimental conditions are same as in Fig. 1.

Fig. 5. Experimental data (symbols), microkinetic model performance (red and black lines) and calculated equilibrium conversion profile (dashed blue line) for SO_2 oxidation on Pt/Al_2O_3 monolith. Solid black and red lines show the model simulations with SO_3 in the experimental feed compositions, dashed black and red lines show the simulations without SO_3 in the feed composition. Operating conditions: [21,12] feed of 100 ppm SO_2, 75 ppm SO_3, 10% O_2, and balance N_2 (red symbols); 149 ppm SO_2, 106 ppm SO_3, 10% O_2, balance N_2 (black symbols). Reactor and catalysts details are same as in Fig. 1. (For interpretation of the references to color in this figure legend, the reader is referred to the web version of the article.)

was chosen. In real conditions, the catalyst surface features (e.g., kinks and step sites) and nature of adsorption of surface species can facilitate the reaction at slightly lower temperatures. There are also challenges modeling the catalysts and parameter space which are discussed later in the model limitation section. Nonetheless, the model predictions are within the experimental error limits ($\delta e < 5\%$). At elevated temperatures (>350 °C), the conversion of SO_2 decreases due to equilibrium limited conditions, consistent with the decrease in calculated equilibrium conversion.

Simulated coverage profiles at the reactor exit over a temperature range of 200–500 °C are shown in Fig. 2. One can see that SO_3^* coverage is dominant at low temperatures. O^* is the most abundant surface species over much of the temperature range, as expected, due to the high concentration of O_2 in the diesel engine exhaust. A small decrease in the O^* coverage at the highest temperatures (>500 °C) is attributed to the onset of desorption of surface oxygen. Empty sites tend to appear and rapidly increase after 400 °C.

Fig. 3 shows the low and high temperature (320 °C and 520 °C) surface coverage profiles over the reactor length. At both temperatures, O^* remains as a dominant surface species, which justifies
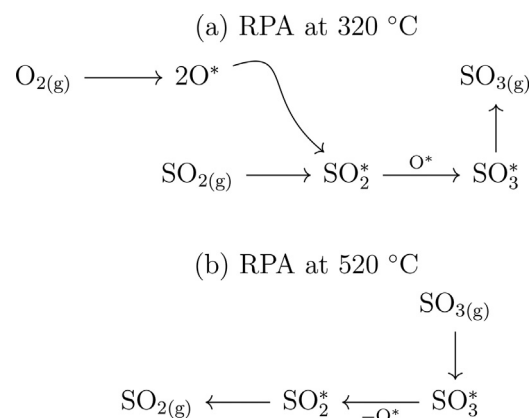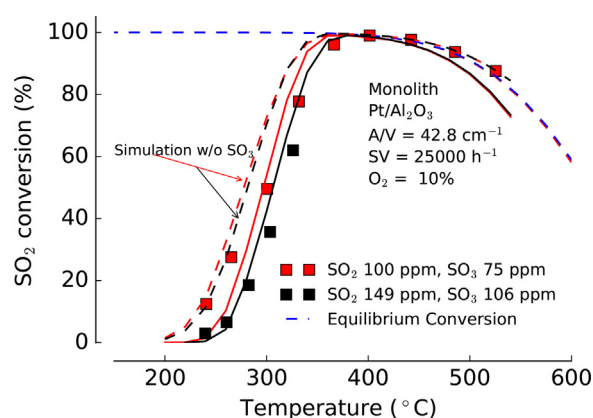
the inclusion of repulsive adsorbate–adsorbate (O^*–O^*) interactions (i.e., coverage effects) in our reaction mechanism. Reaction path analysis (RPA) is shown in Fig. 4 for the two representative temperatures (i.e., 320 °C and 520 °C). It shows that the oxidation of SO_2 (R_{12}, $SO_2^* + O^* \rightarrow SO_3^* + *$) occurs to form SO_3^* on the surface at low temperature which desorbs afterwards. At the higher temperature SO_3 re-adsorption and decomposition occurs via the reverse reaction (R_{11}, $SO_3^* + * \rightarrow SO_2^* + O^*$), consistent with equilibrium limitations.

3.2. Effect of SO_3 on SO_2 oxidation

Experimental study suggested that the presence of SO_3 in the feed severely affects SO_2 oxidation. Kinetic analysis suggested an increase in apparent activation energy with negative reaction order for SO_3 [12]. Light-off temperature (i.e., the reaction initiation temperature) of SO_2 oxidation shifts to higher temperature and SO_2 conversion decreases sharply in the equilibrium-limited region due to SO_3 in the feed. These phenomena are well captured by our model as it correctly predicts the experimental conversion profile of SO_2 oxidation in the presence of SO_3 in the feed. The model performance
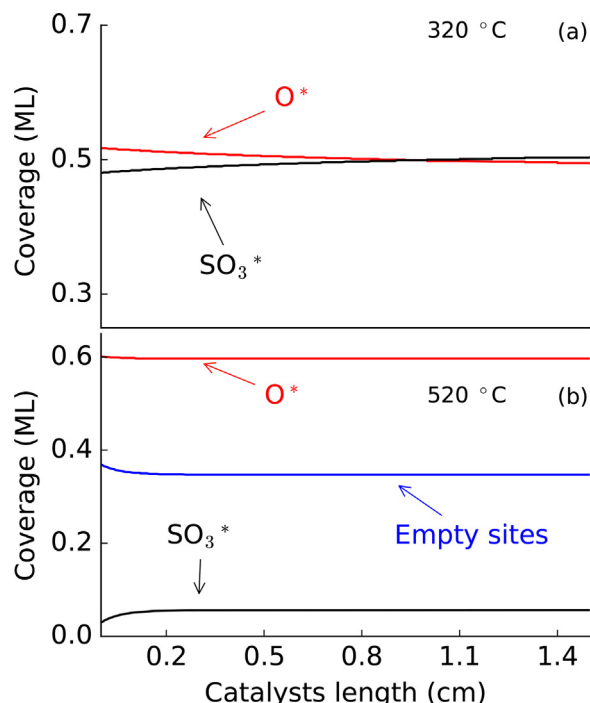
Fig. 6. Simulated axial coverage profiles at (a) 320 °C and (b) 520 °C, respectively for the feed composition of 100 ppm SO_2, 75 ppm SO_3, 10% O_2, balance N_2. Actual catalyst length is 3.86 cm. Experimental conditions are same as in Fig. 5.

against two sets of experimental data [21,12] (obtained from two different feed concentrations of SO_2 and SO_3) is shown in Fig. 5.

To further evaluate the effect of SO_3 on SO_2 conversion in a highly oxidizing environment, both experimental data sets without SO_3 in the inlet feed (i.e., hypothetical conditions) were simulated. The conversion profiles are shown in Fig. 5, as represented by black and red dotted lines. Two distinct features were clearly observable. First, SO_2 concentration change only has minimal effect on the light-off temperature, which shows negligible change in the conversion profiles from 100 ppm (red dashed line) to 149 ppm (black dashed line) of SO_2 in the feed. Second, an increase in SO_3 concentration creates a large shift in the light-off temperature. A negative impact of SO_3 in the feed on SO_2 conversion was observed in the equilibrium limited region, which is consistent with experimental results.

Fig. 6 shows the surface coverage profiles versus catalyst length at two different representative temperatures (at 320 °C and 520 °C). These profiles are very similar to ones without SO_3 (Fig. 3). However, SO_3^* coverage is slightly higher on the surface at both temperatures and O^* still remains as the most dominant species on the surface. Overall, the reaction pathways and mechanisms remain the same in the presence or absence of SO_3 in the feed.

3.3. H_2SO_4 formation

Experimental data for H_2SO_4 formation in the presence of H_2O in engine exhaust conditions is very limited due to the corrosive and toxic nature of H_2SO_4. Here, the monolith-scale experiments reported by Hamzehlouyan et al. on Pt/Al$_2$O$_3$ catalysts were used [21]. Experimental results showed significant decrease in SO_2 conversion in the presence of H_2O which is due to catalysts poisoning by H_2SO_4. The model captures these experimental results, albeit, with a minor adjustment in the catalyst area per unit volume (A/V) parameter. By simulating the conversion profiles using a range of A/V numbers in Fig. 7 one can clearly see the impact on the SO_2 conversion profile, especially at the higher temperatures. H_2SO_4
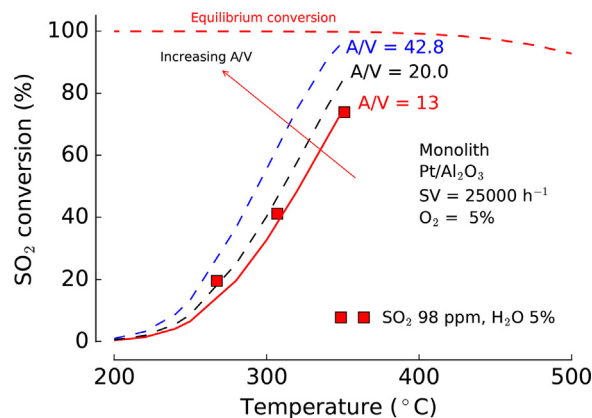

Fig. 7. Experimental data (symbols) and microkinetic model (lines) for H_2SO_4 formation on Pt/Al$_2$O$_3$ monolith. Dotted blue and black lines represent the effect of A/V parameter on the model performance for the prediction of SO_2 conversion data. Operating conditions: [21] feed of 98 ppm SO_2, 5% H_2O, 5% O_2, and balance N_2. Reactor and catalysts details are same as in Fig. 1.
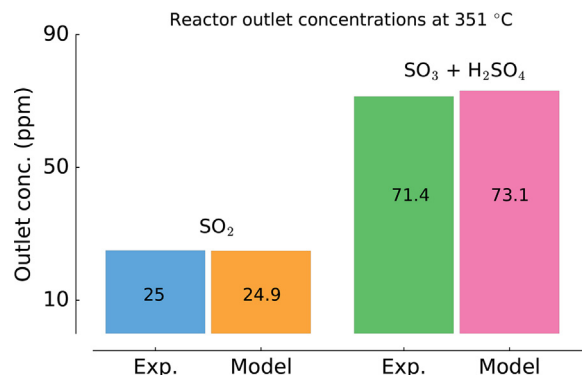

Fig. 8. Comparison of the experimental and model reactor outlet concentrations (at 351 °C) predicted by the microkinetic model.

poisoning of a catalyst reduces the active sites, which is effectively the same as reducing the A/V parameter. It is noted that the plug flow reactor model and mechanism used here is only applicable for fresh catalysts and cannot inherently capture effects due to catalyst poisoning. Thus, minor parameter adjustment in our model is reasonable and within the experimental error margin. To further validate the model, selectivity was computed and compared the model-simulated results against experimentally observed concentrations of the reactants and products at the reactor exit as shown in Fig. 8. The model captures the reactant (SO_2) and the total product (SO_3 and H_2SO_4) concentrations reported at 351 °C in the experiments [21].

Sensitivity analysis allows us to identify the most important reactions. The normalized sensitivity coefficient is defined as $dlnR/dlnP$, where $dlnP$ is the change in parameter P (pre-exponential factor) and $dlnR$ is the change in model response R (SO_2 conversion). A pairwise sensitivity analysis was performed by perturbing the pre-exponential factors of both forward and backward reactions with the same factor. The surface reaction pairs with highest sensitivity coefficients are shown in Fig. 9 at four different temperatures ranging from 200 °C to 350 °C. At low temperature (200 °C), the reaction R_5–R_6 ($SO_3 + ^* \leftrightarrow SO_3^*$) shows the greatest sensitivity. In the interval 200–300 °C, reaction pairs R_5–R_6 ($SO_3 + ^* \leftrightarrow SO_3^*$) and R_{11}–R_{12} ($SO_3^* + ^* \leftrightarrow SO_2^* + O^*$) show the largest impact on the mechanism. The reaction pair R_{13}–R_{14} ($H_2SO_4^* + ^* \leftrightarrow SO_3^* + H_2O^*$) is also one of the important reaction pairs over the range of temperature considered here.
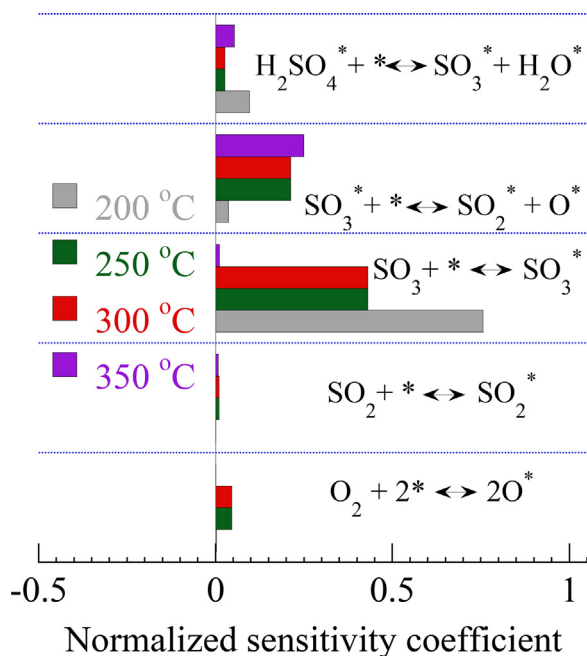
Fig. 9. Sensitivity analysis for the microkinetic model responses with respect to the pre-exponential factor pairs in the surface reaction mechanism shown in Table 1. Pre-exponentials are modified pairwise without perturbing the equilibrium constant. Only those reaction pairs with the highest normalized sensitivity coefficients [$dlnR/dlnP$, i.e., $(dR/dP) \times (P/R)$] are shown here. The sensitivity coefficients at four representative temperatures (i.e., 200 °C, 250 °C, 300 °C, and 350 °C) are shown. Sensitivity analysis at the equilibrium-limited regions is not shown here. Operating conditions are the same as in Fig. 7.

Model-simulated surface coverage profiles on the catalysts at three different temperatures (i.e., 250 °C, 300 °C, and 350 °C) are shown in Fig. 10. The surface species SO_3^* is the MARI at low temperature (250 °C) which is mainly due to its high sticking coefficient (0.5) compared to that of oxygen (0.05). With increasing temperature, the SO_3^* coverage gradually decreases while O^* coverage takes over and becomes the MARI. This effect is partly due to the SO_3^* des-
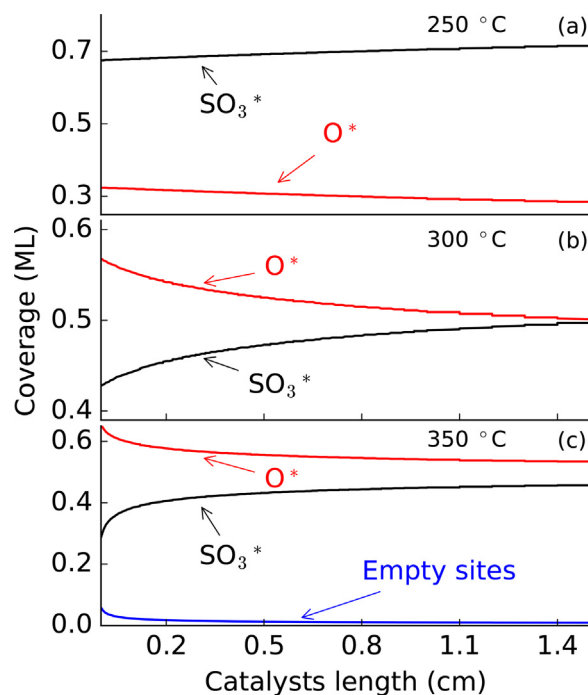

Fig. 10. Comparison of the experimental and model reactor outlet concentrations (at 351 °C) predicted by the microkinetic model.

orption and $H_2SO_4^*$ formation. Furthermore, the binding energy of oxygen is higher than that of SO_3^*, which translates to higher temperature desorption phenomena.

Fig. 11 shows RPA at 250 °C (panel a) and 350 °C (panel b). The lower temperature RPA (at 250 °C) is dominated by SO_2 oxidation ($SO_2^* + ^* \rightarrow SO_3^* + ^*$) and SO_3 desorption ($SO_3^* \leftrightarrow SO_3 + ^*$) steps. However, the higher temperature RPA (at 350 °C) shows that H_2SO_4 formation ($SO_3^* + H_2O^* \rightarrow H_2SO_4^* + ^*$) is a major pathway and competing reaction with SO_3 desorption, which is also consistent with the sensitivity analysis in Fig. 9.
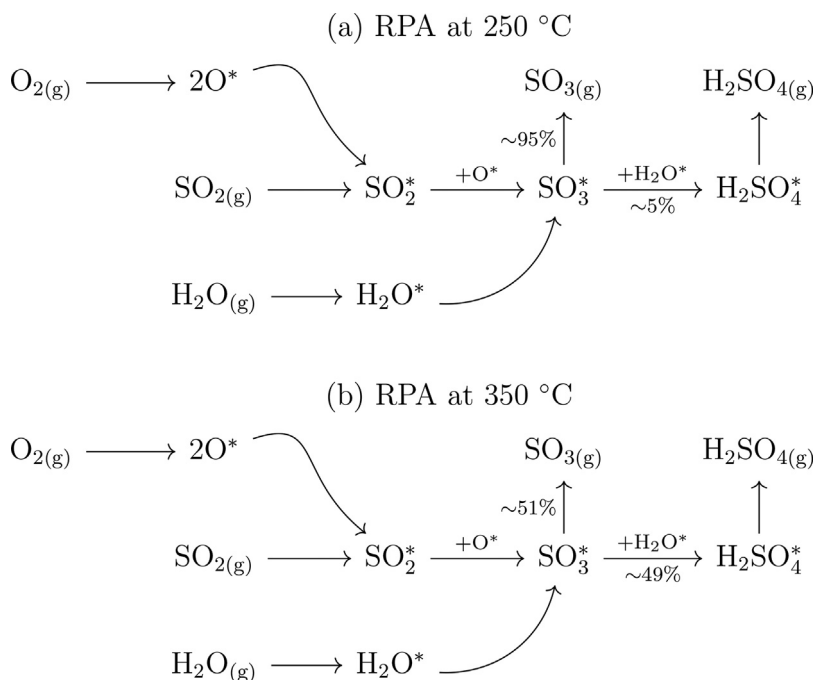

Fig. 11. Reaction path analysis (RPA) at the reactor exit at (a) 250 °C and (b) 350 °C. Experimental conditions are same as in Fig. 7.

4. Model limitations

Some limitations are associated with this modeling approach. The limitations originate primarily from parameter uncertainty due to multiple sources (experiments and DFT) and the semi-empirical UBI-QEP method, mechanistic limitations due to the probable existence of other reactions pathways, and reactor modeling limitations due to the simplistic PFR scheme chosen for the mechanism simulations. Potential effects of the other gas-phase components of diesel engine exhaust (e.g., CO, CO_2, HC, NO_x) are not considered here, which may have some impact on the reaction pathways. Model extension can be done by including possible interaction of SO_x with those species. The model was developed using the (111) surface of Pt; however, the actual catalysts in DOC contain polycrystalline surfaces. Furthermore, the catalyst loading effect is beyond the scope of current study. Further details regarding the limitations associated with aforementioned sources can be found elsewhere [22,28]. Nonetheless, this approach has been used successfully in many prior studies [22,28–32].

5. Conclusions

A microkinetic model was developed for H_2SO_4 formation on Pt(111). The model contains 14 elementary steps (7 reversible pairs) and 5 surface species (i.e., O^*, H_2O^*, SO_2^*, SO_3^*, and $H_2SO_4^*$). The model captures the available experimental data from experiments conducted under realistic DOC conditions such as low emissions concentrations, high oxygen concentrations with presence of water, atmospheric pressure, and high space velocity and shows good agreement in kinetically and thermodynamically controlled regions. The impact of SO_3 on the SO_2 oxidation light-off temperature was analyzed, which is consistent with experimental observations. A sensitivity analysis further shows the important reactions in the proposed mechanism. Finally, the reaction between SO_3 and H_2O was identified to be the primary pathway for H_2SO_4 formation on the Pt surface.

Acknowledgements

Appendix A. UBI-QEP activation energy computation

To calculate activation energies using the UBI-QEP [19,20] method, a thermodynamic loop with gas phase and surface reactions is considered. Here, activation barrier for HSO_3^* formation from SO_3^* and OH^* was shown as mentioned earlier in the main text. Further details regarding the method and activation barrier computation for different types of reactions can be found elsewhere [8,22].

To calculate the activation energies based on the UBI-QEP method, the surface reaction for HSO_3^* formation reaction is actually written in the endothermic direction for the corresponding gas phase, i.e., $HSO_3^* + ^* \leftrightarrow SO_2^* + OH^*$. For the reaction loop considered, the heat of surface reaction can be calculated as:

$$\Delta H_{surf} = D_{gas} + Q_{SO_3} - Q_{SO_2} - Q_{OH} \qquad (A.1)$$

where D_{gas} and Q represent the gas phase bond dissociation energy and the binding energy of the species, respectively. D_{gas} (23.02 kcal mol^{-1}) is calculated from the reactant and product enthalpies. In this work, the thermodynamic database [26,33] was used to compute enthalpies.

The forward activation energy, using UBI-QEP formalism, is given by,

$$E_f = w \left[\Delta H + \frac{Q_{SO_2} Q_{OH}}{Q_{SO_2} + Q_{OH}} \right] \qquad (A.2)$$

where w is the bond index, which loosely translates to the location of transition state with respect to reactants and products. The range of bond index is from 0 to 1 (with a typical value of 0.5). Then, backward activation energy is calculated as:

$$E_b = E_f - \Delta H_{surf} \qquad (A.3)$$

with $\Delta H_{surf} = -32.58$ kcal mol^{-1}, $Q_{HSO_3} = 36.8$ kcal mol^{-1}, $Q_{SO_2} = 29.39$ kcal mol^{-1}, $Q_{OH} = 63.0$ kcal mol^{-1}, and $w = 0.5$, the HSO_3^* decomposition activation energy (E_f) and formation activation energy (E_b) (after UBI-QEP adjustment for negative E_f) [19,34] at 300 K is calculated to be 0.0 kcal mol^{-1} and 32.6 kcal mol^{-1}, respectively.

Appendix B. DFT calculations

Our first-principles density functional theory (DFT) calculations were performed using the efficient plane wave basis code Vienna ab initio Simulation Package (VASP) [24,25] employing the Perdew, Burke and Ernzerhof [35] exchange-correlation functional and the projector augmented-wave methodology [36]. A plane-wave cutoff energy of 400 eV was used for the plane-wave expansion of the wave functions. The Pt(111) surfaces was represented by a five-layer slab and a (3×3) surface unit cell. The two bottom layers of the slab were fixed, and the other layers were allowed to relax. An intervening 12–14 Å vacuum region was introduced to avoid any periodic image interactions. Monkhorst–Pack grids [37] of $4 \times 4 \times 1$ were used to sample the Brillouin zone. The energy of a single atom

a. HSO_3 b. H_2SO_4

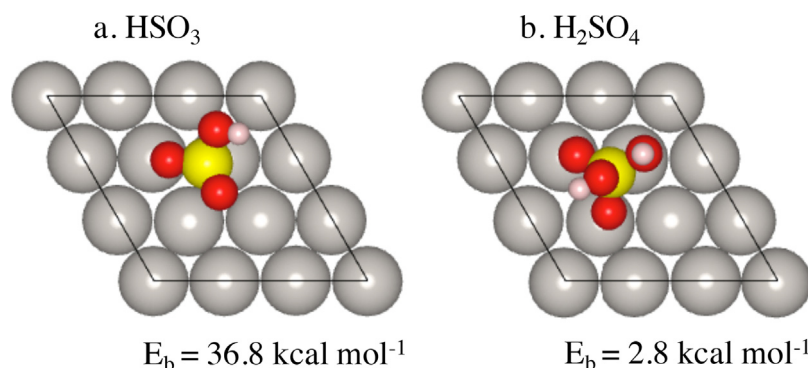$E_b = 36.8$ kcal mol^{-1} $E_b = 2.8$ kcal mol^{-1}

Fig. B.12. Most stable structural models and DFT computed binding energies of HSO_3^* and $H_2SO_4^*$ on Pt(111) surface.

or molecule was calculated using a $14 \times 14 \times 14\,\text{Å}^3$ cell. Finally, convergence in optimizing the structures was assumed when the Hellman–Feynman forces become less than $0.01\,\text{eV}\,\text{Å}^{-1}$.

The binding energy, E_b, of an atom or a molecule on the slab is defined as:

$$E_b = -[E_{\text{slab+adsorbate}} - E_{\text{slab}} - E_{\text{adsorbate}}] \tag{B.1}$$

where $E_{\text{slab+adsorbate}}$, E_{slab}, and $E_{\text{adsorbate}}$ represent the energy of the slab with the atom/molecule, energy of the clean slab, and the energy of an isolated atom/molecule, respectively. The computed binding energies of the most stable configurations of HSO_3 and H_2SO_4 for a surface coverage of 0.11 ML were found to be $36.8\,\text{kcal}\,\text{mol}^{-1}$ and $2.8\,\text{kcal}\,\text{mol}^{-1}$, respectively. Structural models are shown in Fig. B.12.

References

[1] O. Kröcher, M. Widmer, M. Elsener, D. Rothe, Ind. Eng. Chem. Res. 48 (2009) 9847–9857.
[2] R.J. Farrauto, K.E. Voss, Appl. Catal. B 10 (1996) 29–51.
[3] A. Russell, W.S. Epling, Catal. Rev. 53 (2011) 337–423.
[4] G. Corro, React. Kinet. Catal. Lett. 75 (2002) 89–106.
[5] B.M. Penetrante, R.M. Brusasco, B.T. Merritt, G.E. Vogtlin, Sulfur Tolerance of Selective Partial Oxidation of NO to NO₂ in a Plasma, Technical Report 1999-01-3687, Lawrence Livermore National Laboratory, 1999.
[6] H.N. Sharma, S.L. Suib, A.B. Mhadeshwar, Interactions of Sulfur Oxides With Diesel Oxidation Catalysts (DOCs), volume 1132 of Novel Materials for Catalysis and Fuels Processing, American Chemical Society, Washington, DC, 2013, pp. 117–155.
[7] P.J.S. Oswald Kubaschewski, C.B. Alcock, Materials Thermochemistry, 6th ed., Pergamon Press, Oxford/New York, 1993, Rev. ed. of: Metallurgical Thermochemistry. 5th ed., rev. and enl. 1979.
[8] H.N. Sharma, V. Sharma, T. Hamzehlouyan, W. Epling, A.B. Mhadeshwar, R. Ramprasad, J. Phys. Chem. C 118 (2014) 6934–6940.
[9] H.N. Sharma, V. Sharma, A.B. Mhadeshwar, R. Ramprasad, J. Phys. Chem. Lett. 6 (2015) 1140–1148.
[10] J.A. Phillips, M. Canagaratna, H. Goodfriend, K.R. Leopold, J. Phys. Chem. 99 (1995) 501–504.
[11] E.R. Lovejoy, J. Curtius, K.D. Froyd, J. Geophys. Res. D: Atmos. 109 (2004) D08204.
[12] T. Hamzehlouyan, C. Sampara, J. Li, A. Kumar, W. Epling, Appl. Catal. B 152–153 (2014) 108–116.
[13] J. Dawody, M. Skoglundh, L. Olsson, E. Fridell, Appl. Catal. B 70 (2007) 179–188.
[14] W.R. Pierson, R.H. Hammerle, J.T. Kummer, SAE International, 1974, pp. 740287.
[15] R.J. Kriek, J. Rossmeisl, S. Siahrostami, M.E. Bjorketun, Phys. Chem. Chem. Phys. 16 (2014) 9572–9579.
[16] W. Benzinger, A. Wenka, R. Dittmeyer, Appl. Catal. A 397 (2011) 209–217.
[17] H. Somnitz, G. Gleitsmann, R. Zellner, Proceedings of the AAC-Conference (2003) 19–24.
[18] J.M. Standard, I.S. Buckner, D.H. Pulsifer, J. Mol. Struct. 673 (2004) 1–16.
[19] E. Shustorovich, H. Sellers, Surf. Sci. Rep. 31 (1998) 1–119.
[20] H. Sellers, E. Shustorovich, Surf. Sci. 356 (1996) 209–221.
[21] T. Hamzehlouyan, C. Sampara, J. Li, A. Kumar, W. Epling, SO₂ oxidation over Pt/Al₂O₃ catalysts, 2013 (accessed 30.09.13) http://cleers.org/workshops/workshop2013/index.php.
[22] H.N. Sharma, A.B. Mhadeshwar, Appl. Catal. B 127 (2012) 190–204.
[23] J.A. Dumesic, D.F. Rudd, L.M. Aparicio, J.E. Rekoske, A.A. Trevino, The Microkinetics of Heterogeneous Catalysis, 1st ed., American Chemical Society, 1993.
[24] G. Kresse, J. Furthmüller, Phys. Rev. B 54 (1996) 11169.
[25] G. Kresse, J. Furthmüller, Comput. Mater. Sci. 6 (1996) 15–50.
[26] G.P. Smith, D.M. Golden, M. Frenklach, N.W. Moriarty, B. Eiteneer, M. Goldenberg, C.T. Bowman, R.K. Hanson, S. Song, W.C. Gardiner, V.V. Lissianski, Z. Qin, Gri-mech 3.0, 1999.
[27] S. Li, L. Petzold, Design of new DASPK for Sensitivity Analysis, 1999.
[28] M. Koehle, A. Mhadeshwar, Chem. Eng. Sci. 78 (2012) 209–225.
[29] A.B. Mhadeshwar, H. Wang, D.G. Vlachos, J. Phys. Chem. B 107 (2003) 12721–12733.
[30] A.B. Mhadeshwar, J.R. Kitchin, M.A. Barteau, D.G. Vlachos, Catal. Lett. 96 (2004) 13–22.
[31] A.B. Mhadeshwar, D.G. Vlachos, Combust. Flame 142 (2005) 289–298.
[32] M. Salciccioli, M. Stamatakis, S. Caratzoulas, D.G. Vlachos, Chem. Eng. Sci. 66 (2011) 4319–4355.
[33] E. Goos, A. Burcat, B. Ruscic, DAT, 2015 (accessed 10.07.15) http://garfield.chem.elte.hu/Burcat/THERM.
[34] A. Mhadeshwar, A Hierarchical Multiscale Approach for Predictive Microkinetic Modeling of Hydrogen Production, University of Delaware, Newark, DE, 2005 (Ph. D. thesis).
[35] J.P. Perdew, K. Burke, M. Ernzerhof, Phys. Rev. Lett. 77 (1996) 3865–3868.
[36] P.E. Blöchl, Phys. Rev. B 50 (1994) 17953–17979.
[37] H.J. Monkhorst, J.D. Pack, Phys. Rev. B 13 (1976) 5188–5192.